CHEMHIST, connecting structure and function from organisms to molecules in small animal symbioses through chemo-histo-tomography

Benedikt Geier[1]; Janina Oetjen[2]; Bernhard Ruthensteiner[3]; Maxim Polikarpov[4]; Harald Gruber-Vodicka[1]; Manuel Liebeke[1]*

[1]Department of Symbiosis, Max Planck Institute for Marine Microbiology, Bremen, Germany

[2]MALDI Imaging Lab, University of Bremen, Bremen, Germany

[3]SNSB The Bavarian State Collection of Zoology, Munich, Germany

[4]European Molecular Biology Laboratory, Hamburg Unit c/o Deutsches Elektronen-Synchrotron, Hamburg, Germany

Abstract

Our understanding of the metabolites involved in the interactions between small symbiotic animals and bacteria or other eukaryotes that reside within their body is extremely limited. This gap in knowledge originates from a methodological challenge, namely to connect metabolites to the histological changes in host tissues throughout colonization and persistence of beneficial and parasitic (micro)organisms in situ.

To close this gap, we developed chemo-histo-tomography (CHEMHIST), a culture-independent approach to connect anatomic structure and metabolic function in millimeter-sized symbiotic animals. CHEMHIST combines spatial metabolomics based on mass spectrometry imaging (MSI) and microanatomy-based micro-computed X-ray tomography (microCT) on the same animal. Both high-resolution MSI and microCT allowed us to correlate the distribution of metabolites to the same animal's three-dimensional (3D) histology down to sub-micrometer resolutions. Building CHEMHIST upon in situ imaging approaches, we sampled an earthworm from its natural habitat and created an interactive 3D model of its physical and chemical interactions with bacteria and parasitic nematodes in its tissues. Our CHEMHIST protocol is compatible with other molecular techniques, which include tissue specific DNA sequencing and localization of bacteria using fluorescence in situ hybridization (FISH) to complement the spatial metabolomics data.

We demonstrate on an earthworm, a key species for soil ecosystem-functioning across the globe that combining MSI and microCT offers a powerful platform to connect metabolic and anatomic phenotypes of small symbiotic animals in situ.

Significance

Metabolites mediate the establishment and persistence of most inter-kingdom symbioses. However, the cellular- and organ-scale distributions of the metabolites involved in the symbiotic interactions in animals remain poorly understood. This gap originates from a missing link between anatomic structure and metabolic function at different life stages of symbiotic animals, such as the developmental and colonization status of the host. We addressed this problem by developing a culture-independent imaging approach termed chemo-histo-tomography (CHEMHIST), which combines micro-computed X-ray tomography and mass spectrometry imaging as key technologies. With CHEMHIST we created a 3D snapshot of an earthworm, connecting its anatomic phenotype and spatial chemistry, which revealed its metabolic interactions with symbiotic bacteria and parasitic nematodes in situ.

Introduction

Earthworms are a key species in soil ecosystems across the globe (1) and a prime example of a small symbiotic animal that experiences constant chemical interactions with the environment and other organisms. Soil as a habitat represents an ever-changing landscape, a mixture of small molecules, metabolites produced by bacteria (2), fungi (3), plants, and small invertebrates, such as nematodes (4). Earthworms are constantly exposed to this set of external metabolites, which also pass through their digestive system with the detritus and soil particles (5). In addition to the metabolites in their food, symbiotic microbes and small animals that reside in the earthworms' tissues provide an additional metabolic interactions inside the host.

Nearly all lumbricid earthworms harbor species-specific bacteria in a loop of their excretory organs, called the ampulla (6). Although the symbiotic bacteria increase the host fitness, it is unclear if the symbionts complement the host through the biosynthesis of vitamins or the detoxification of nitrogenous waste products (7). In addition to the symbiotic microbes, nematodes, the most abundant animals on earth (4), form commensal and parasitic symbioses with earthworms. The nematodes reside in the muscles, blood vessels and excretory organs of earthworms and use them as intermediate and sole hosts (8). The interactions between earthworms and nematodes have been described across

species for centuries, but the chemical interactions between these two key organisms of soil ecosystems have remained unstudied.

The sum of mutualistic, commensal and pathogenic interactions results in a unique anatomic and in particular, metabolic phenotype for nearly every host individual (9). The ability to connect metabolic with anatomic phenotypes of host and symbiont tissues in the same host animal could allow us to disentangle how the interactions between the symbiotic partners affect metabolic heterogeneity (10). Previous studies have addressed this methodological challenge by combining non-destructive magnet resonance tomography (MRT) with matrix-assisted laser desorption/ionization (MALDI)-MSI to connect the spatial chemistry and 3D anatomy of organs (11) and pathogenic abscesses (12, 13) of the same animals. The resolution used in these approaches was ideal for imaging animals in the size range of tens of centimeters, with millimeter-sized organs. However, the majority of animals used as symbiosis models (14) have body sizes that span only a few millimeters, and thus contain organs with microbial symbionts that require imaging at micro- to nanometer resolutions. Additionally, these methodological advances where established for the study of mouse-bacterial pathogen models that can be cultured and genetically modified (11-13, 15). However, the physical and chemical interactions of symbiotic organisms in their habitat result in phenotypes that are almost impossible to reproduce in the laboratory and therefore require culture-independent in situ imaging techniques (16).

Micro-computed tomography (microCT) is a non-invasive approach allowing X-ray imaging of 3D histology, and unlike MRT, microCT can reach subcellular resolution (17-20). Similarly, MALDI-MSI techniques can now reach subcellular resolution (21, 22). Combining microCT and MALDI-MSI would thus seem an ideal approach to visualize an animal's 3D histology and spatial chemistry at micrometer scales, yet the techniques have almost exclusively been applied independently (23). The principal obstacles are that MSI requires tissue sectioning and thus cannot be applied before 3D imaging of the anatomy, whereas microCT conventionally requires chemical contrasting of soft tissues (24), which would change the chemistry of the sample and interfere with subsequent MSI (25).

Here we present **chem**o-**his**to-**t**omography 'CHEMHIST' that combines MALDI-MSI and microCT to image both the spatial chemistry and 3D microanatomy of the same small symbiotic animal. Our

objective was to make CHEMHIST also applicable to animals that cannot be cultured in the laboratory. By integrating state-of-the-art in situ imaging approaches within one pipeline, CHEMHIST provides an up to two orders of magnitude higher resolution than previous correlative 3D MALDI-MSI approaches. This allowed us to sample an earthworm from the environment and visualize its 3D chemical and physical interactions with bacteria and nematodes naturally occurring inside its tissues.

Results and Discussion

CHEMHIST workflow

CHEMHIST consists of three major steps. First, we physically divided the same animal for the different fixation and sample preparation procedures of MSI and microCT (Fig. 1A). Second, we created a combined 3D overview of the spatial chemistry and anatomy of the animal's posterior end. Applying MSI and microCT at moderate resolutions, sufficient to resolve organs from tens to hundreds of micrometers, instead of high-spatial resolutions allowed faster imaging at larger fields of view (e.g. whole cross sections of an animal with MSI). We combined the imaging data to create a 3D model of the spatial chemistry and anatomy at a whole animal and organ scale. In the third step, we analyzed the combined chemo-histo 3D model to determine regions of interest, such as associated bacteria or parasites in the animal tissue that we imaged with high-resolution MSI and microCT. Because we use the CHEMHIST 3D model as an overview to guide the high-resolution measurements, we referred to the 3D model as an atlas.

To apply MSI and microCT to the same animal, here an earthworm (*Lumbricus rubellus*), we had to treat the sample in a manner that preserves both morphology and spatial chemistry, but without one technique interfering with the other. For CHEMHIST, snap-freezing provided a tradeoff between preserving enough anatomic details for microCT without modifying the spatial chemistry for MALDI-MSI. For microCT and MALDI-MSI we divided our frozen sample into two sample types: tissue blocks (1–3 millimeter-thick), trimmed off the frozen sample with a razor blade and tissue sections (16 µm thick), sectioned off each tissue block with a cryotome (Fig. 1A). We obtained tissue blocks for microCT and tissue sections for MSI. Additionally, we stored consecutive tissue sections from in between the tissue blocks for high-resolution MSI and spatially targeted metagenomics sequencing.

Obtaining both sample types in an alternating manner provided sample pairs of one tissue block for microCT and one adjacent tissue section for MSI (Fig. 1). Sharing the same sectioning interface, each tissue section anatomically and chemically matched its adjacent tissue block, which allowed us to precisely correlate microCT and MALDI-MSI data despite segregating the tissues. We documented the position of each tissue block and tissue section along the length of the animal, which we used afterwards as an estimate to reconstruct the 3D CHEMHIST atlas (Fig. 1A and *SI Appendix*, Fig. S-1). Dividing the frozen sample, allowed us to chemically post-fix the tissue blocks intended for microCT with paraformaldehyde and osmium tetroxide. Thereby, we could minimize the tissue damage induced by thawing and preserve subcellular detail for high-resolution microCT (Fig. 3 A–E). To generate an anatomic 3D atlas, we imaged each of the five tissue blocks with microCT at a 4.4 µm voxel size. From the five microCT datasets, we virtually reconstructed a 3D anatomy model of the specimen (Fig. 1B and 3A, *SI Appendix*, Fig. S-2). To gain an overview of the spatial chemistry throughout the sample, we imaged four cryo-sections with MALDI time-of-flight (TOF)-MSI at a 25-µm pixel size (*SI Appendix*, Fig. S-3). After MALDI-TOF-MSI we used bright-field microscopy and fluorescence in situ hybridization (FISH) to image the histology and the bacteria in each of the four tissue sections (10)(Fig. 2 and *SI Appendix*, Fig. S-4). To complete the 3D CHEMHIST atlas, we co-registered the 2D imaging MALDI-TOF-MSI, FISH and bright-field microscopy datasets into the anatomic 3D model (Fig. 1B, *Appendix*, Fig. S-2). Using the 3D imaging platform AMIRA© provided a graphical user interface to visualize and co-register 3D and 2D imaging data (*SI Appendix*, Video S1).

Finally, we analyzed the 3D anatomy (Fig. 1C and E) with the spatial chemistry on an organ scale (Fig. 1D and F) to guide high-resolution imaging (Fig. 3) and DNA extractions for metagenomics sequencing of specific tissue regions (*SI Appendix*, Figure S-5). Our analysis of the microCT data indicated micrometer-scale worms (~ 20–30 µm in diameter) in the earthworm tissues. We chose these small worms to showcase how CHEMHIST can be used to guide high-resolution microCT, MSI and metagenomics sequencing to resolve their anatomy and spatial chemistry and taxonomically identify them as parasitic nematodes. Synchrotron radiation-based (SR)microCT allowed us to rescan specific regions of the same tissue blocks and resolve subcellular structures at an eleven times increased resolution (0.325 µm voxel size), (Fig. 3A and B). To determine the metabolite production of single

nematodes, we imaged a region of a consecutive tissue section to one of the MALDI-TOF MSI datasets (Fig. 3F–K) with atmospheric pressure (AP)-MALDI-orbitrap-MSI. This high-resolution MSI technique provided a spatial resolution of 8-µm pixel size and a higher mass accuracy below 3 ppm, allowing for more precise metabolite annotations. Both the SRmicroCT and AP-MALDI-orbitrap-MSI datasets were co-registered into the 3D atlas, providing different levels of resolution of the same structures (Fig. 3A and C).
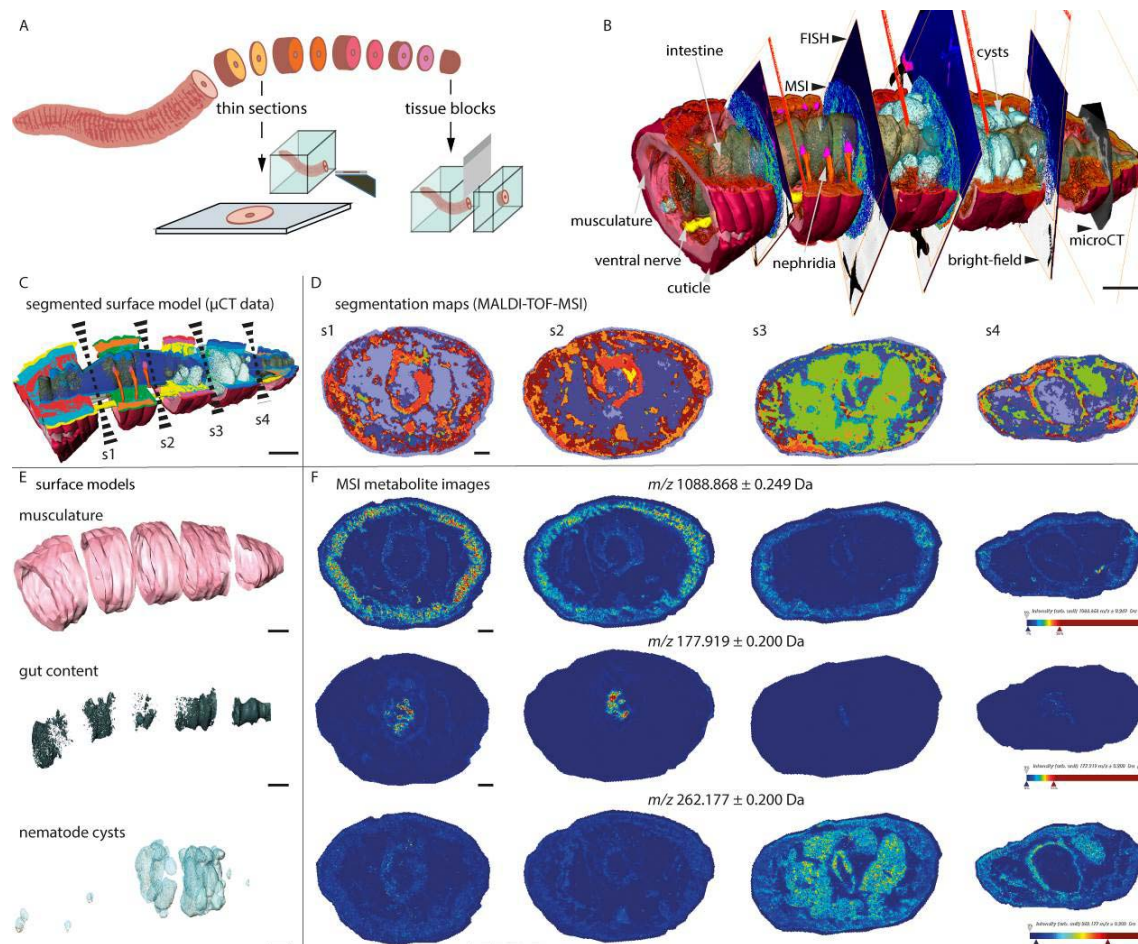

Fig. 1: Chemo-histo-tomography (CHEMHIST) applied to the posterior segments of an earthworm. A) Division of the tissue into alternating thin-sections for spatial metabolomics and microscopy and tissue blocks for tomography. **B)** 3D CHEMHIST atlas at organ-scale with data from microCT, MALDI-TOF-MSI, FISH and bright-field microscopy. **C)** Segmentation of the 3D microCT data (surface models, semi-automatic segmentation) and **D)** 2D MALDI-TOF-MSI data to delineate the spatial chemistry (unsupervised spatial metabolite clustering). Sectioning planes of sections s1–s4 indicated in **C** with dashed wedge. **E)** Examples of surface models of individual organs and **F)** individual metabolites located in the organ throughout sections s1–s4. Scale bars in **B**, **C** and **E**: 2000 µm (2D scale bars in 3D models as approximate scale) and magnifications in **F**: 500 µm.

CHEMHIST provides a cross-kingdom link between spatial chemistry and 3D anatomy

The specific chemistry of an organ is intimately linked to its functioning, such as in movement, digestion or signal transduction. To study the association between organ-specific metabolites and 3D anatomy of the earthworm, we visualized the spatial chemistry through segmentation maps of metabolite clusters and the 3D anatomy with surface models (Fig. 1C–F). We obtained the metabolite clusters through unsupervised spatial clustering (26) and the 3D surface models by semi-automatic segmentation based on grey values of microCT data. Comparing the segmentation maps of the metabolite clusters and the individually segmented organs allowed us connect anatomic structure and metabolic function.

The anatomical segmentation of earthworms provides a modularly repeated anatomy and thus a great target organism for developing CHEMHIST, as it allows repeated observations of the same organ in different sections and identify irregularities in the chemical and anatomic phenotype of the animal. In this earthworm dataset, we consistently located specific metabolites in tissue cross-sections of continuous organs over the length of the animal, such as musculature and gut content (Fig. 1F). For example, in the musculature, we located lombricine with (AP)-MALDI-orbitrap-MSI (*m/z* 271.0802, $[C_6H_{15}N_4O_6P\square+\square H]\square$) an annelid specific energy storage metabolite (27) (*SI Appendix*, Table S-1). In the earthworm's body wall, we detected protoporphyrin (*m/z* 563.2653, $[C_{34}H_{34}N_4O_4\square+\square H]\square$), a typical pigment in the dorsal epidermis of lumbricid earthworms (28) (*SI Appendix*, Table S-1). Covering larger volumes of tissue, the 3D microCT data allowed a precise localization of discontinuous organs, such as the nephridia that are not present in each tissue section used for MSI. The 3D CHEMHIST atlas helped us to identify histological structures that originated from sectioning planes through the discontinuous organs and appeared infrequently. We could identify the earthworm's nephridia in the 3D microCT data (Fig. 1B and 2A), which occur pairwise in each segment and harbor symbiotic bacteria (6, 7). Using correlative MSI and FISH microscopy (10) on tissue sections, we were able to visualize only parts of the nephridia, including the bacteria within the organ after labeling them with specific fluorescent probes for bacteria (Fig. 2A, D and E). Although the nephridia did not show a distinct metabolite cluster, we used the fluorescence signals to filter and

determine colocalized metabolite distributions from the MSI data (Fig. 2B and C) (*SI Appendix*, Fig. S-4) (10). The 3D CHEMHIST atlas of a field-collected earthworm also allowed us to understand structures that are not part of an earthworm's anatomic bauplan (blueprint). In the earthworm's coelomic cavity, we found cysts filled with nematodes. We used a spatially targeted tissue extraction, which yielded material for sequencing DNA. We sequenced and identified the nematodes in the earthworm tissue as *Rhabditis maupasi* (*SI Appendix*, Fig. S-5). This species are known parasites that reside in the earthworms' nephridia and coelomic cavities for example of *Lumbricus terrestris*, *Lumbricus rubellus*, *Allobophora longa*, and *Allobophora turgid* (29). The cysts increased in size and density toward the posterior of the earthworm, where they almost completely filled the coelomic cavity (Fig. 1B and 3A, *SI Appendix*, Fig. S-6). These nematode-filled cysts possessed a specific chemistry characterized by a spatial metabolite cluster (Fig. 1B, C, F and 2A).
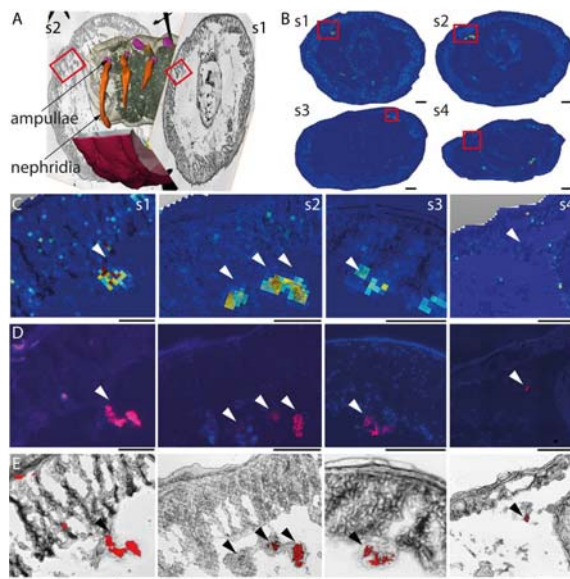

Fig. 2: Bacterial cells within organs have unique molecular fingerprints. A) The 3D model shows the surface reconstruction of the nephridia, including the bacteria-containing ampullae, of the second tissue piece between tissue section s1 and s2. **B)** The ion images of whole tissue sections show the metabolite *m/z* 1116.833, found through the colocalization analysis of MALDI-MSI and FISH signals. Red boxes in s1–s4 indicate magnified areas, shown as MSI and bright-field overlay in **C). D)** FISH microscopy images and **E)** FISH and bright-field overlay with bacteria labeled in red. Scale bars of whole tissue sections s1–s4 (**B**): 500 µm and magnifications in **C–E**: 250 µm.

Guiding high-resolution MSI and microCT to visualize host–parasite interactions with CHEMHIST

To demonstrate the combination of high-resolution MSI and microCT, we visualized the interactions between parasitic nematodes and earthworms by connecting their metabolic and anatomic phenotypes. The observed cysts are known as brown bodies and produced by earthworms to encapsulate organic debris, microbes and parasites to chemically degrade them using reactive oxygen species (30, 31). Our 3D CHEMHIST atlas clearly showed the distinct anatomy and spatial chemistry of the brown bodies that encapsulated the nematodes. Directing micrometer-scale metabolite imaging (Fig. 3 A–E) and nanometer-scale histology (Fig. 3 F–K) towards the brown bodies of the same animal allowed us to spatially resolve the physical and metabolic interactions between individual nematodes and the earthworm's cells.

In the brown body tissue, the nanometer-scale histology (SRmicroCT) data showed distinct physiological states of the nematodes, known from live animals (32). We found nematodes that contained highly electron-dense inclusions and nematodes that were in the process of disintegrating into a granular mass, indicating degradation caused by the earthworm (Fig. 3D and E, *SI Appendix*, Fig. S-6) (32). We also found histologically intact nematodes, some of which were surrounded by a homogeneous deposit (Fig. 3D and E). This deposit was hypothesized to be a humoral response of the earthworm against the nematodes in the coelomic cavity (33). Similar to the distribution of this deposit, the micrometer-scale metabolite images revealed that most nematodes were surrounded by a platelet activation factor (PAF), specifically lysophosphatidylcholine (lysoPC) O-16:0/0:0 (*m/z* 482.3605, $[C_{24}H_{52}NO_6P\square+\square H]\square$) (Fig. 3J, *SI Appendix*, Fig. S-7 and Table S-1). PAFs are single fatty acid chain phospholipids that serve as inflammatory modulators in metazoans across all domains of life (34). In the earthworm, PAF lipids and their structural analogues are part of the humoral immune response (35). This lysoPC(O-16:0/0:0) accumulating around the nematodes could promote aggregation of hemocytes (36), which form most of the brown body tissue (31, 33) and their release of reactive oxygen species (37). Although it is likely that the earthworm produced PAF as an

inflammatory response, from the imaging data we cannot exclude that the PAFs could have originated
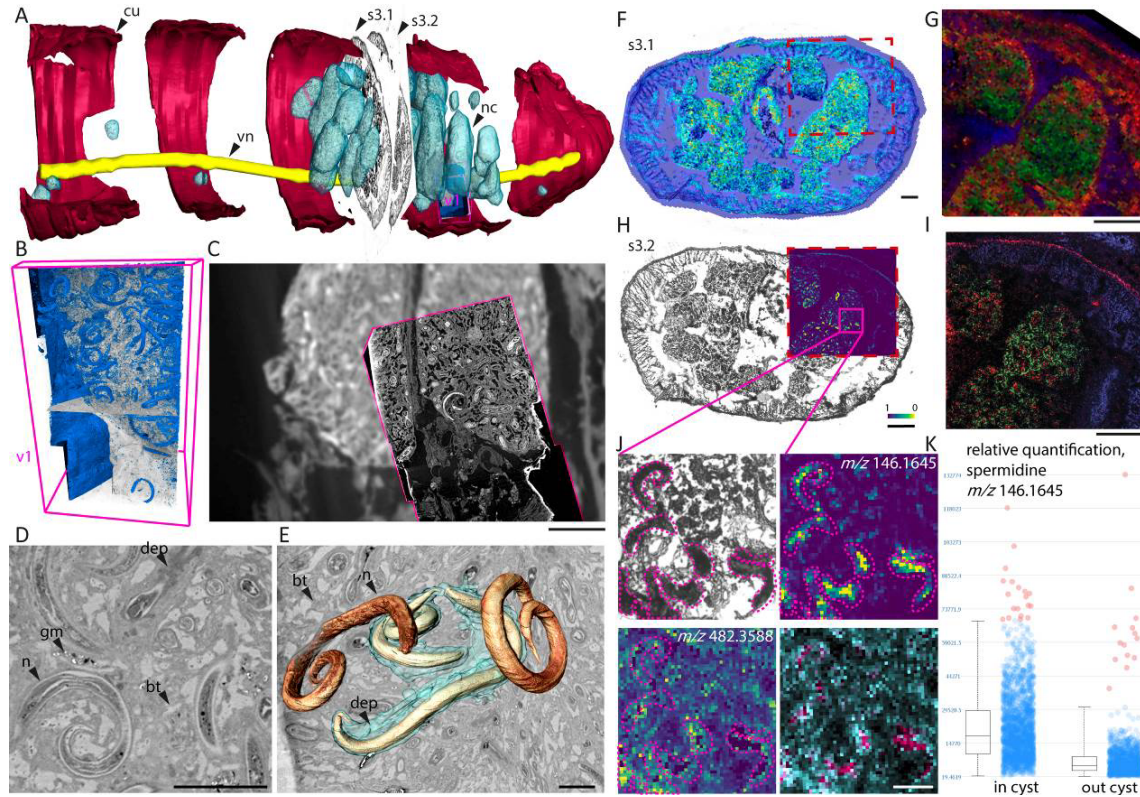
form the nematodes.

Fig. 3: Using the 3D CHEMHIST atlas to guide high-resolution imaging of the interactions between earthworm and nematodes in 3D. A) microCT model with the co-registered MSI sections (s3.1 and s3.2) and the tissue volume (v1) imaged with high-resolution SRmicroCT. **B)** Isosurface 3D rendering of the nematodes (blue) and a virtual sectioning plane (*xy*) through the SRmicroCT image stack. **C)** Overlay of the microCT and SRmicroCT (magenta outline, *xy*-plane) to show the increased resolution and detail gained with SRmicroCT. **D)** Magnified plane through the SRmicroCT data and **E)** 3D rendering of four nematodes, with two nematodes surrounded by a homogeneous deposit (cyan). **F–J)** MALDI-MSI datasets, of **F)** a whole cross-section (s3.1) imaged with **G)** MALDI-TOF-MSI (25 µm pixel size, *m/z* 262.178 Da) and **H)** a specific area (s3.2) imaged with **I)** AP-SMALDI-MSI (8 µm pixel size, distribution of *m/z* 262.0601 Da). Red dashed squares in (s3.1) and (s3.2) indicate a comparable field of view of the same brown body cyst to illustrate the improvement in resolution from MALDI-TOF-MSI **(G)** and AP-SMALDI-orbitrap-MSI **(I). J)** Magnified bright-field image shows the nematodes (magenta outlines) in a cyst, the distributions of PAF (*m/z* 482.3588, cyan) and spermidine (*m/z* 146.1645, magenta) and overlaid with PAF in cyan and spermidine in magenta. **K)** Relative quantification of spermidine in nematodes in- and outside the brown body cysts. **cu**, cuticle; **nc**, nematode cyst; **vn**, ventral nerve cord; **n**, nematode; **dep**, deposit; **bt**, brown body

tissue; **gm**, granular mass; **i**, electron dense inclusions. Scale bars in C: 500 µm, in D and F (same as H): 100 µm, E and J (all four panels): 25 µm, G and I: 150 µm.

Focusing on the metabolite profiles of the nematodes, we detected higher levels of the polyamine spermidine (m/z 146.1652, $[C_7H_{19}N_3\square+\square H]\square$) in nematodes within the brown body cysts than in nematodes outside of brown bodies (Fig. 3K, *SI Appendix*, Fig. S-7, S-8 and Table S-1). Spermidine supplementation in other nematodes enhances longevity, inducing autophagy and suppressing oxidative stress and necrosis (38). The nematodes encapsulated in brown bodies might increase their levels of spermidine to inhibit necrosis, as a protection against the reactive oxygen species of the earthworm. Surviving in the brown bodies until the earthworm sheds its posterior segments via autotomy (39) might firstly provide an escape mechanism, and secondly a substrate for the nematodes, which reach maturity once the earthworm tissue begins to decay (32, 40).

Conclusion

Faced with the intimidating complexity of natural systems, scientists have studied model organisms under controlled conditions and so gained an understanding of their detailed molecular biology. This meticulous research on model organisms has created a strong foundation of databases and new technologies. Today, this groundwork allows us to leave the laboratory and tease apart the array of molecular interactions and their effects on the phenotypic heterogeneity of organisms in nature. CHEMHIST allowed us to visualize a 3D chemical and anatomical snapshot of the interactions between an animal and its parasites and taxonomically identify the associated species.

Notably, CHEMHIST requires an elaborate workflow and access to state-of-the-art devices that is difficult to extend for a large sample size at the moment (e.g. hundreds of specimens). In exchange, CHEMHIST offers an unprecedented in-depth analysis of millimeter-sized symbiotic animals and their in-situ interactions with (micro)organisms without prior knowledge of the sample. The correlative data provides a new perspective by connecting anatomic structure and metabolic function to generate hypotheses on how metabolites with known functions could serve a different purpose during the interactions of organisms in their natural habitat.

Extending the field of histotomography (19) into chemo-histo-tomography (CHEMHIST) opens uncharted territory for label-free correlative imaging. Although our approach provided a wealth of biological and biochemical information, dividing the sample for the separate techniques led to a minimal loss of tissue and potentially relevant details. Future development of CHEMHIST could integrate phase-contrast SRmicroCT (41), an emerging technique that allows quantitative 3D imaging of tissues without contrasting agents at nanometer scales (42, 43). Serial MSI after phase-contrast SRmicroCT would provide data for a lossless anatomic and metabolic 3D model of the same organism (44) and the basis for automated correlations between modalities in 3D (45).

We envision that our advances in correlative chemical and structural in situ imaging will drive discovery-based research and fuel scientists' hypotheses on the metabolic interactions of their symbiotic systems, sampled in their natural habitat.

Materials and Methods

Chemicals and reagents

All chemicals were obtained from Sigma-Aldrich (Steinheim, Germany) unless specified otherwise.

Tissues and sample collection

An adult earthworm (*Lumbricus rubellus*) was collected from soil in a polder region of the central Netherlands (supplied by Lasebo BV, Netherlands) and rapidly frozen in isopentane cooled with liquid nitrogen. The posterior end (30 segments, approx. 2 cm) was embedded in 2% carboxymethylcellulose (CMC) gel and subsequently solidified at -20 °C. Using a precooled razor blade, the embedded earthworm was trimmed inside a cryo-chamber. Sectioning of the frozen sample block was performed as follows. The first tissue section (1–3 mm) was cut with a razor blade from the frozen CMC block. The block was then trimmed and several 16 µm sections were obtained with a cryotome (-20 °C). This was repeated to obtain five blocks of tissue and four adjacent thin sections. Thin sections were transferred onto Bruker® ITO glass slides via thaw mounting. Small crosses (1–2 mm) were drawn around the dried samples using a white paint marker (edding ®751) as a reference for the computational alignment (46). The slides were stored at 4 °C prior to MSI matrix application. The

tissue blocks were used for microCT measurements and the adjacent thin sections for correlative bright-field microscopy, MSI and FISH imaging.

Micro-computed tomography

The frozen tissue blocks were defrosted in 8% paraformaldehyde. Contrasting was achieved using an aqueous 1% osmium tetroxide/acetone (1:1 vol./vol.) solution for 2.5 h at 20 °C. Dehydration and infiltration were conducted according to the 45345 FLUKA Epoxy embedding medium data sheet. The resin blocks were pre-trimmed with a fretsaw, then fine trimmed using a razor blade (47). Trimmed embedded earthworm tissue blocks were mounted individually on glass rods with a hot-melt gun. A "nanotom m" computed tomography system (GE Measurement & Control, Wunstorf, Germany) was used for the microCT analysis of the tissue blocks with the following X-ray parameters: 110 kV, 120 µA, 0.75 s exposure time, averaging = 4, scanning time = 1.5 h, number of projections acquired during scan = 1500. The tomographic reconstruction was performed using the phoenix datos|x 2.2 reconstruction software (GE Measurement & Control, Wunstorf, Germany) on a separate workstation and resulted in a voxel size of 4.4 µm. The 16-bit volume is saved in *.vgl format. This format was imported into the 3D-visualization software VGStudio (2.2) (Volume Graphics, Heidelberg). Cropping, histogram adjustments, bit dept (to 8 bit) and format (to *.raw volume) conversions were performed in VGStudio.

Synchrotron radiation-based micro-computed phase-contrast X-ray tomography
P14 beamline. After determining the position of the encysted nematodes in the laboratory-based microCT data, one small tissue block (~ $1 \times 1 \times 3$ mm) was cropped out from tissue block 3 with a razor blade in an area that contained the nematodes. The cropped out block was mounted onto one SPINE sample holder (48). Experiments were carried out on the EMBL undulator beamline P14 at the PETRA-III storage ring (c/o DESY, Hamburg, Germany) using the propagation-based phase-contrast imaging setup described in (49, 50). X-ray energy of 18 keV was used. The X-ray images were obtained using an X-ray microscope (Optique Peter, Lyon , France) consisting of an LSO:Tb scintillator with a thin active layer of 8 µm, an OLYMPUS UPlanFL 20-fold objective lens (Olympus,

Tokyo, Japan), a 45°-reflecting mirror, an OLYMPUS 180 mm Tube Lens and PCO.edge 4.2 sCMOS camera with a 2048×2048 pixels sensor at a pixel size of 6.5 µm. The effective pixel size of 0.325 µm resulted in a 666×666 µm^2 field of view. To ensure artifact-less phase retrieval (51) in the near-field edge-enhancing regime, each tomographic acquisition consisted of four measurements at sample-to-detector distances of 5.9, 6.4, 7, and 7.9 cm. A total of 1850 projections covering 185 degrees of continuous rotation and 40 flat-field images were acquired at each distance with a frame rate of 100 frames per second. A complete four-distance tomographic data acquisition took less than 2 minutes. Three tomograms with overlapping areas were acquired along the vertically shifted sample.

SRmicroCT Data processing

Data processing was carried out using in-house Python software, performing flat-field correction, phase retrieval and tomographic reconstruction. First, each X-ray image of the sample was divided by the flat-field image with the highest similarity. For this operation, we used the similarity index (SSIM) implemented in the scikit-image Python module as a metric (52). Subsequently, a four-distance non-iterative holographic reconstruction procedure (53) was applied with a δ/β ratio of 0.17 to obtain a projected phase map of the sample at the given angle. The tomographic reconstruction was then performed using the tomopy Python module (54) with 'gridrec' algorithm and 'shepp-logan' filter. The three reconstructed volumes were co-registered with the commercial software Amira 6.7.0 (Thermo Fisher Scientific, USA), which did not require any non-linear operations, because we used the transform editor.

MALDI-TOF-MSI

For MALDI-MSI, a matrix consisting of 7 mg mL^{-1} α-cyano-4-hydroxycinnamic acid in 70:30 acetonitrile/water with 0.2% trifluoroacetic acid was applied via an automated spray-coating system (SunCollect, SunChrom GmbH, Germany) using the following parameters: *z*-distance of the capillary 25 mm; pressure of compressed air 2 bar; the flow for the first layer was 15 µL min^{-1} and for layers 2–8 20 µl min^{-1}.

MALDI-MS imaging was performed using an Autoflex speed™ LRF MALDI-TOF (Bruker Daltonik, Germany) with MALDI Perpetual™ ion source and smartbeam™-II 1 kHz laser and reflector analysis in positive modes (11). A spot size of 25 µm was used and 500 shots per sampling point acquired using a "random walk" pattern with 100 shots per location within the sampling spot. The mass detection range was set to *m/z* 100–1280 with 200 ppm accuracy. For data processing and visualization of the MALDI-MS imaging data, flexImaging™ 4.0 (Bruker Daltonik, Germany, 2015) was used.

AP-MALDI-orbitrap-MSI

High spatial resolution MSI was performed using an atmospheric-pressure scanning microprobe MALDI source (AP-SMALDI10®, TransMIT GmbH, Giessen, Germany) with a Q Exactive™ plus Fourier transform orbital trapping mass spectrometer (Thermo Scientific, Germany). A nitrogen laser with a wavelength of 337 nm and 60 Hz repletion rate was used for desorption and ionization. The laser beam was focused to an 8 µm ablation spot diameter and a step size of 8 µm in *x* and *y* was used to scan the sample. Mass spectral acquisition was performed in positive mode and *m/z* 100–1000 Da with a mass resolving power of 140,000 (dataset in Fig. 3) at 200 *m/z* with a mass accuracy <5 ppm. Additional datasets for the annotation of metabolites in METASPACE (55) and MS/MS experiments were recorded with a resolving power of 240,000 (see *SI Appendix* Table S-1) at 200 *m/z* with a mass accuracy <5 ppm. The mass spectrometer was set to automatic gain control, fixed to 500 ms injection time. For data processing and visualization, ImageQuest 1.1 (Thermo Scientific) was used.

MALDI-MS[2]

The identification of spermidine and PAF was supported by MALDI-MS[2] experiments (*SI Appendix*, Table S-1 and Figure S-9). For PAF we obtained enough ions to use on tissue MALDI-MS[2] in positive-ion mode with the mass analyzer set to a resolution of 240k resolution and a collision energy of 25 eV in the HCD cell. For spermidine, we could not obtain sufficient ions from the tissue to perform on tissue fragmentation. To support the identification of the exact mass, we matched the MS[1] *m/z* values of spermidine measured from the tissue with the MS[1] *m/z* values from a spermidine standard. The standard was spotted onto a glass slide and fragmented with MALDI-MS[2], in positive-

ion mode with the mass analyzer set to a resolution of 240.000 resolution and a collision energy of 30 eV in the HCD cell.

MALDI-MSI data analysis and visualization

The *.raw files were centroided and converted to *.mzML with MSConvert GUI (ProteoWizard, version 3.0.9810 (56)) and then to *.imzML using the imzML Converter 1.3 (57). SCiLS Lab software (SCiLS, Bruker Daltonik GmbH, Bremen, Germany) version 2019b was used for spatial segmentation analysis and alignment of bright-field microscopy and MSI datasets as a template for ROI selection.

DNA extraction and metagenomics sequencing

Genomic DNA was extracted using the DNeasy Blood & Tissue Kit (Qiagen, Hilden, Germany). In brief, the nematode cysts from one consecutive tissue section of tissue section s3 (*SI Appendix*, Fig. S-5) were scraped off the glass slide using a sterile scalpel and transferred into a tube containing 180 μl buffer ATL and 20 μl proteinase K. The tissue was digested at 56°C for 3 days. Subsequent extraction steps were performed according to the manufacturer's instructions. In the end 100 μl elution buffer were applied to the column and incubated at room temperature for 10 min. After the first round of elution, a second elution 100 μl of buffer was performed and the two elutions were pooled. The extracted DNA was stored at 4°C until further processing.

llumina-library preparation and sequencing were performed by the Max Planck Genome Centre. In brief, DNA quality was assessed with the Agilent 2100 Bioanalyzer (Agilent) and genomic DNA was fragmented to an average fragment size of 400 base pairs (bp). An Illumina-compatible library was prepared using the TPase-based DNA library protocol. One nanogram of genomic DNA was cut and specific sequences were introduced by the Illumina Tagment DNA Enzyme (Illumina). Products were amplified by KAPA 2G Robust polymerase (Roche) with 15 cycles to enrich and to add library-specific barcoding information to the PCR products. After quality check by LabChip GX II (Perkin Elmer) libraries were pooled and sequenced on an Illumina HiSeq3000 sequencer with 2 x 150 bp paired end mode. Three million 150 bp paired-end reads were sequenced on a HiSeq 3000 (Illumina).

Parasitic nematode phylogenetic analyses using the small subunit rRNA gene

We used phyloFlash v3.3 beta1 (https://github.com/HRGV/phyloFlash) (58) to assemble full-length SSU genes from the metagenomic reads. The nematode SSU matrix was constructed from the assembled *Rhabditis* related sequence, the available full length SSU genes of all species level representatives of the *Rhabditis* group and *Teratorhabditis* sequences as an outgroup. The sequences were aligned using MAFFT v7.394 (59) in G-Insi mode. The phylogenetic tree was reconstructed using FastTree v2.1.5 (60) with a GTR model, 20 rate categories and Gamma20 likelihood optimization, generating approximate likelihood-ratio-test values for node support. The tree was drawn with Geneious R11 (https://www.geneious.com) and rooted with *Teratorhabditis* as an outgroup.

Fluorescence in-situ hybridization and bright-field microscopy

After MALDI-MS imaging, the matrix was removed by dipping the sample slide into 70% ethanol and 30% water (vol./vol.) for 1 min each. In a second step, the tissue sections were post-fixed for one hour at 4°C in 2% paraformaldehyde in PBS. The sample was dried under ambient conditions and then prepared for catalyzed reporter deposition fluorescence in situ hybridization (CARD-FISH) following ref (61). For in situ hybridization, general probes were used that target conserved regions of the 16S rRNA in bacteria (EUB338; I-III; I: 5'-GCT GCC TCC CGT AGG AGT-3', II: 5'-GCA GCC ACC CGT AGG TGT-3', III: 5'-GCT GCC ACC CGT AGG TGT-3') (62, 63). To visualize tissue containing DNA, samples were stained for nuclei with DAPI for 10 min. at room temperature, washed three times for 1 minute and mounted in a VECTASHIELD®/Citiflour® mixture (2:11) with 1 part PBS (pH 9) under a cover slip (Menzel glass, 24 × 60 mm, #1.5). Image acquisition for individual photomicrographs was carried out using a Zeiss Axioplan 2 microscope.

To image large sections for bright-field and fluorescence microscopy at high resolution, an automated microscope (Zeiss Axio Imager Z2.m, 10× objective) with a tile-scan Macro for Axio Vision was used. Individual images were acquired with 15% overlap and stitched (Fiji Plugin stitching 1.1).

Composition of the 3D atlas

To combine the different modalities into the 3D atlas, tools in Amira 6.7.0 were used for segmentation, surface rendering and 3D co-registration (47). The individual microCT volumes were imported as *.raw files and manually realigned, based on the estimations of the location and composition of shared morphological features. Exact spacing of the intervals between tissue blocks relied on an estimate, as the precise thickness of tissue used for the sections could not be recorded due to loss of tissue during sectioning. However, information about the overall number of the earthworm segments allowed a realistic reconstruction of the overall spatial relations of the specimen. Subsequently, the light microscopy images were co-registered into the spaces between tissue blocks, using morphologic structures in the orthographic cross-section of the microCT data as a template. Based on the previous alignment of the 2D-imaging modalities in SCiLS Lab, the co-registration parameters could be applied to the FISH- and MALDI-imaging data. All 3D visualizations and applications with high computation demands were performed using a 3D-imaging workstation (Windows 7 Professional, 64 bit, Intel Core i7-5960X CPU with 16 processors $\times$ 3.5 GHz, 64 GB RAM and NVIDIA Quadro P6000 with 24 GB).

Author Contributions

BG and ML conceived the study. BG prepared all the samples and together with BR acquired the laboratory based microCT. MP acquired and reconstructed the SRmicroCT data. 3D and 2D visualizations and the co-registrations in Amira were done by BG. HGV coordinated metagenomics sequencing and analyzed the data. JO acquired the MALDI-TOF-MSI datasets and BG acquired the AP-MALDI-orbitrap-MSI dataset and FISH microscopy. The analysis of the MSI data in SCiLS Lab was done by BG.. The manuscript and the figures were drafted and edited by BG and ML. All authors edited and commented on the manuscript.

Corresponding Author* Dr. Manuel Liebeke, Department of Symbiosis, Max Planck Institute for Marine Microbiology, Celsiusstraße 1, 28359 Bremen, Germany

email: mliebeke@mpi-bremen.de

Phone: +49 (0) 421-20 28 822

Notes

The authors declare no competing financial interest.

Data availability

All datasets (MSI, microCT and microscopy) can be accessed and directly downloaded under:

https://figshare.com/projects/CHEMHIST_connecting_structure_and_function_from_organisms_to_m

olecules_in_small_animal_symbioses_through_chemo-histo-tomography/73527

A video animation of the multimodal 3D atlas can be found here:

https://figshare.com/articles/media/final_mpg/4003944

Acknowledgements

References

1. N. Fierer, Earthworms' place on Earth. *Science* **366**, 425-426 (2019).
2. M. Delgado-Baquerizo *et al.*, A global atlas of the dominant bacteria found in soil. *Science* **359**, 320-325 (2018).
3. L. Tedersoo *et al.*, FUNGAL BIOGEOGRAPHY. Response to Comment on "Global diversity and geography of soil fungi". *Science* **349**, 936 (2015).
4. J. van den Hoogen *et al.*, Soil nematode abundance and functional group composition at a global scale. *Nature* **572**, 194-198 (2019).
5. M. Liebeke *et al.*, Unique metabolites protect earthworms against plant polyphenols. *Nature Communications* **6** (2015).
6. S. K. Davidson, D. A. Stahl, Transmission of nephridial bacteria of the earthworm Eisenia fetida. *Appl Environ Microbiol* **72**, 769-775 (2006).
7. M. B. Lund, M. Holmstrup, B. A. Lomstein, C. Damgaard, A. Schramm, Beneficial Effect of Verminephrobacter Nephridial Symbionts on the Fitness of the Earthworm Aporrectodea tuberculata. *Appl Environ Microbiol* **76**, 4738-4743 (2010).
8. G. O. Poinar, Associations between Nematodes (Nematoda) and Oligochaetes (Annelida). *Proceedings of the Helminthological Society of Washington* **45**, 202-210 (1978).
9. V. V. Phelan, W. T. Liu, K. Pogliano, P. C. Dorrestein, Microbial metabolic exchange-the chemotype-to-phenotype link. *Nature Chemical Biology* **8**, 26-35 (2012).
10. B. Geier *et al.*, Spatial metabolomics of in situ host-microbe interactions at the micrometre scale. *Nat Microbiol* 10.1038/s41564-019-0664-6 (2020).
11. J. Oetjen *et al.*, MRI-compatible pipeline for three-dimensional MALDI imaging mass spectrometry using PAXgene fixation. *Journal of Proteomics* **90**, 52-60 (2013).

12. A. S. Attia *et al.*, Monitoring the Inflammatory Response to Infection through the Integration of MALDI IMS and MRI. *Cell Host Microbe* **11**, 664-673 (2012).

13. J. E. Cassat *et al.*, Integrated molecular imaging reveals tissue heterogeneity driving host-pathogen interactions. *Science Translational Medicine* **10** (2018).

14. A. E. Douglas, Simple animal models for microbiome research. *Nat Rev Microbiol* **17**, 764-775 (2019).

15. T. K. Sinha *et al.*, Integrating spatially resolved three-dimensional MALDI IMS with in vivo magnetic resonance imaging. *Nature Methods* **5**, 57-59 (2008).

16. J. Alfred, I. T. Baldwin, New opportunities at the wild frontier. *eLife* **4** (2015).

17. M. Topperwien, F. van der Meer, C. Stadelmann, T. Salditt, Three-dimensional virtual histology of human cerebellum by X-ray phase-contrast tomography. *P Natl Acad Sci USA* **115**, 6940-6945 (2018).

18. M. Muller *et al.*, Myoanatomy of the velvet worm leg revealed by laboratory-based nanofocus X-ray source tomography. *P Natl Acad Sci USA* **114**, 12378-12383 (2017).

19. Y. F. Ding *et al.*, Computational 3D histological phenotyping of whole zebrafish by X-ray histotomograhpy. *eLife* **8** (2019).

20. M. Busse *et al.*, Three-dimensional virtual histology enabled through cytoplasm-specific X-ray stain for microscopic and nanoscopic computed tomography. *P Natl Acad Sci USA* **115**, 2293-2298 (2018).

21. M. Kompauer, S. Heiles, B. Spengler, Atmospheric pressure MALDI mass spectrometry imaging of tissues and cells at 1.4-mu m lateral resolution. *Nat Methods* **14**, 90-96 (2017).

22. M. Niehaus, J. Soltwisch, M. E. Belov, K. Dreisewerd, Transmission-mode MALDI-2 mass spectrometry imaging of cells and tissues at subcellular resolution. *Nat Methods* **16**, 925-931 (2019).

23. F. Bollenbeck, S. Kaspar, H. P. Mock, D. Weier, U. Seiffert, Three-Dimensional Multimodality Modelling by Integration of High-Resolution Interindividual Atlases and Functional MALDI-IMS Data. *Lect N Bioinformat* **5462**, 126-+ (2009).

24. R. Fernandez, S. Kvist, J. Lenihan, G. Giribet, A. Ziegler, Sine systemate chaos? A versatile tool for earthworm taxonomy: non-destructive imaging of freshly fixed and museum specimens using micro-computed tomography. *Plos One* **9**, e96617 (2014).

25. X. Xu *et al.*, A brief review on mass/optical spectrometry for imaging analysis of biological samples. *Applied Spectroscopy Reviews* **54**, 57-85 (2019).

26. H. Thiele *et al.*, 2D and 3D MALDI-imaging: conceptual strategies for visualization and data mining. *Biochim Biophys Acta* **1844**, 117-137 (2014).

27. R. J. Rossiter, T. J. Gaffney, H. Rosenberg, A. H. Ennor, The formation in vivo of lombricine in the earthworm (Megascolides cameroni). *Biochem J* **76**, 603-610 (1960).

28. A. E. Needham, Distribution of protoporphyrin, ferrihaem and Indoles in the Body-Wall of L. Terrestris. *Comparative Biochemistry and Physiology* **Vol. 26**, 429-442 (1968).

29. C. G. Goodchild, G. H. Irwin, Occurrence of Nematodes Rhabditis anomala and R. pellio in Oligochaetes Lumbricus rubellus and L. terrestris. *Transactions of the American Microscopical Society* **90**, 231-237 (1971).

30. P. S. Valembois, J.; Lassègues, M., Evidence of lipofuscin and melanin in the brown body of the earthworm Eisenia fetida andrei. *Cell Tissue Research* **277**, 183–188 (1994).

31. P. Valembois, M. Lassegues, P. Roch, Formation of brown bodies in the coelomic cavity of the earthworm Eisenia fetida andrei and attendant changes in shape and adhesive capacity of constitutive cells. *Dev Comp Immunol* **16**, 95-101 (1992).

32. G. O. Poinar, G. M. Thomas, Rhabditis pellio Schneider (nematoda) from the earthworm, Aporrectodea trapezoides Duges (Annelida). *J Nematol* **7**, 374-379 (1975).

33. G. O. H. Poinar, R.T. , "Immune Responses in the Earthworm, Aporrectodea trapezoides (Annelida), Against Rhabditis pellio (Nematoda)" in Comparative Pathobiology*, B. L. A. C. T.C., Ed. (Springer, Boston, MA, 1977), vol. 3, pp. 69-84.

34. T. Sugiura, T. Fukuda, T. Miyamoto, K. Waku, Distribution of alkyl and alkenyl ether-linked phospholipids and platelet-activating factor-like lipid in various species of invertebrates. *Biochimica et Biophysica Acta (BBA) - Lipids and Lipid Metabolism* **1126**, 298-308 (1992).

35. T. Sugiura *et al.*, Platelet-activating factor and its structural analogues in the earthworm Eisenia foetida. *Biochimica et biophysica acta* **1258**, 19-26 (1995).

36. E. S. Garcia, D. P. Castro, M. B. Figueiredo, F. A. Genta, P. Azambuja, Trypanosoma rangeli: a new perspective for studying the modulation of immune reactions of Rhodnius prolixus. *Parasit Vectors* **2**, 33 (2009).

37. R. A. Quinn *et al.*, Correction to 'Metabolomics of reef benthic interactions reveals a bioactive lipid involved in coral defence'. *Proc Biol Sci* **283** (2016).

38. T. Eisenberg *et al.*, Induction of autophagy by spermidine promotes longevity. *Nat Cell Biol* **11**, 1305-1314 (2009).

39. D. Keilin, Parasitic Autotomy of the Host as a mode of liberation of Coelomic Parasites from the Body of the Earthworm. *Parasitology* **17**, 170-172 (1925).

40. J. A. Somers, H. H. Shorey, L. K. Gaston, Reproductive-Biology and Behavior of Rhabditis-Pellio-(Schneider) (Rhabditida-Rhabditidae). *J Nematol* **9**, 143-148 (1977).

41. A. Snigirev, I. Snigireva, V. Kohn, S. Kuznetsov, I. Schelokov, On the possibilities of x☐ray phase contrast microimaging by coherent high☐energy synchrotron radiation. *Review of Scientific Instruments* **66**, 5486-5492 (1995).

42. O. Betz *et al.*, Imaging applications of synchrotron X-ray phase-contrast microtomography in biological morphology and biomaterials science. 1. General aspects of the technique and its advantages in the analysis of millimetre-sized arthropod structure. *Journal of Microscopy* **227**, 51-71 (2007).

43.   J. Herzen *et al.*, 3D grating-based X-ray phase-contrast computed tomography for high-resolution quantitative assessment of cartilage: An experimental feasibility study with 3T MRI, 7T MRI and biomechanical correlation. *Plos One* **14** (2019).

44.   B. Geier *et al.*, *Correlative 3D anatomy and spatial chemistry in animal-microbe symbioses: developing sample preparation for phase-contrast synchrotron radiation based micro-computed tomography and mass spectrometry imaging*, SPIE Optical Engineering + Applications (SPIE, 2019), vol. 11113.

45.   R. Van de Plas, J. Yang, J. Spraggins, R. M. Caprioli, Image fusion of mass spectrometry and microscopy: a multimodality paradigm for molecular tissue mapping. *Nature Methods* **12**, 366-372 (2015).

46.   M. Kaltenpoth, K. Strupat, A. Svatos, Linking metabolite production to taxonomic identity in environmental samples by (MA)LDI-FISH. *Isme Journal* **10**, 527-531 (2016).

47.   S. Handschuh, N. Baeumler, T. Schwaha, B. Ruthensteiner, A correlative approach for combining microCT, light and transmission electron microscopy in a single 3D scenario. *Front Zool* **10** (2013).

48.   F. Cipriani *et al.*, Automation of sample mounting for macromolecular crystallography. *Acta Crystallogr D* **62**, 1251-1259 (2006).

49.   M. Polikarpov *et al.*, Visualization of protein crystals by high-energy phase-contrast X-ray imaging. *Acta Crystallogr D Struct Biol* **75**, 947-958 (2019).

50.   M. Polikarpov, G. Bourenkov, A. Snigirev, T. Schneider, *High-throughput x-ray imaging, microscopy, and tomography for biological applications on EMBL beamline P14 at PETRA III (Conference Presentation)*, SPIE Optical Engineering + Applications (SPIE, 2019), vol. 11113.

51.   S. Zabler, P. Cloetens, J. P. Guigay, J. Baruchel, M. Schlenker, Optimization of phase contrast imaging using hard x rays. *Rev Sci Instrum* **76** (2005).

52.   Z. Wang, A. C. Bovik, H. R. Sheikh, E. P. Simoncelli, Image quality assessment: From error visibility to structural similarity. *Ieee T Image Process* **13**, 600-612 (2004).

53.   P. Cloetens *et al.*, Holotomography: Quantitative phase tomography with micrometer resolution using hard synchrotron radiation x rays. *Appl Phys Lett* **75**, 2912-2914 (1999).

54.   D. Gursoy, F. De Carlo, X. H. Xiao, C. Jacobsen, TomoPy: a framework for the analysis of synchrotron tomographic data. *J Synchrotron Radiat* **21**, 1188-1193 (2014).

55.   T. Alexandrov *et al.*, METASPACE: A community-populated knowledge base of spatial metabolomes in health and disease. *bioRxiv* 10.1101/539478, 539478 (2019).

56.   M. C. Chambers *et al.*, A cross-platform toolkit for mass spectrometry and proteomics. *Nature Biotechnology* **30**, 918-920 (2012).

57.   A. M. Race, I. B. Styles, J. Bunch, Inclusive sharing of mass spectrometry imaging data requires a converter for all. *Journal of Proteomics* **75**, 5111-5112 (2012).

58.   H. R. Gruber-Vodicka, B. K. B. Seah, E. Pruesse, phyloFlash – Rapid SSU rRNA profiling and targeted assembly from metagenomes. *bioRxiv* 10.1101/521922, 521922 (2019).

59.   K. Katoh, D. M. Standley, MAFFT multiple sequence alignment software version 7: improvements in performance and usability. *Mol Biol Evol* **30**, 772-780 (2013).

60.   M. N. Price, P. S. Dehal, A. P. Arkin, FastTree 2--approximately maximum-likelihood trees for large alignments. *PLoS One* **5**, e9490 (2010).

61.   A. Pernthaler, J. Pernthaler, R. Amann, Fluorescence in situ hybridization and catalyzed reporter deposition for the identification of marine bacteria. *Appl Environ Microbiol* **68**, 3094-3101 (2002).

62.   R. I. Amann *et al.*, Combination of 16s Ribosomal-Rna-Targeted Oligonucleotide Probes with Flow-Cytometry for Analyzing Mixed Microbial-Populations. *Appl Environ Microbiol* **56**, 1919-1925 (1990).

63.   H. Daims, A. Bruhl, R. Amann, K. H. Schleifer, M. Wagner, The domain-specific probe EUB338 is insufficient for the detection of all Bacteria: Development and evaluation of a more comprehensive probe set. *Systematic and Applied Microbiology* **22**, 434-444 (1999).